Wind Tunnel Flow Field Visualizations of the Space Launch System Vehicle Ascent

Theodore J. Garbeff II[*], Jennifer K. Baerny[†], James C. Ross[‡]
NASA Ames Research Center, Moffett Field, Ca, 94035

A series of wind tunnel tests were conducted to characterize the force-and-moment, and aeroacoustic environment of several configurations of the Space Launch System during ascent. The tests were conducted in the 11-by-11 foot transonic and 9-by-7 foot supersonic test sections at NASA Ames research center. Throughout these experiments data was collected from several types of instrumentation including: multicomponent force-and-moment strain gage balances, dynamic and steady-state pressure sensors, unsteady and steady pressure-sensitive paint, time-resolved shadowgraph and infrared imaging. The following details results and analysis from the time-resolved shadowgraph and infrared imaging data systems. The time-resolved shadowgraph and infrared imaging provided a qualitative measurement of the near-field turbulent fluctuations. These results helped provide context to the relative magnitude and frequency content of the fluid-structure-interaction driving the surface pressure phenomena characterized by the discrete pressure transducers and unsteady pressure sensitive paint.

I. Introduction

A wind tunnel test was conducted to characterize the force-and-moment and aeroacoustic environment of several configurations of the Space Launch System (SLS) during ascent. The test was conducted in the 11-by-11 foot transonic and 9-by-7 foot supersonic test sections of the Unitary Plan Wind Tunnel (UPWT) at NASA Ames Research Center. Throughout this experiment data was collected from several types of instrumentation including: multicomponent force-and-moment strain-gage balances, dynamic and steady-state pressure sensors, unsteady and steady pressure-sensitive paint, time-resolved shadowgraph and infrared imaging. The shadowgraph imaging systems at the NASA Ames UPWT consist of both high-speed and low-speed cameras that simultaneously image the flow field. This dual camera configuration produces two data products: a high-speed burst of images, and a high-resolution, long duration movie. The high-speed image burst is typically operates at frame rates on the order of 50,000 with exposure times as low as 4 microseconds. This enables the ability to time-resolve flow features and perform statistical and frequency domain analysis on the flow-field surrounding the vehicle. The low-speed, high-resolution movie captures the content that occurs between set-points as the model moves in angle-of-attack, sideslip, or roll. This is useful for review purposes and can help verify test repeatability or identify low-frequency flow phenomena such as hysteresis. Shadowgraph imagery was captured on every model configuration in each test section at Mach numbers ranging from 0.7 to 2.5. The results presented here will be limited to the 11-by-11 foot test and Mach numbers ranging from subsonic to supersonic (Mach = 0.7 to 1.3).

The deployment and integration of a high-speed camera capability has been shown to extend the classical shadowgraph test technique beyond traditional flow visualization [1]. The ability to time-resolve the structure of complex fluid flows, by imaging at sufficiently high frame rates and low exposure times, reveals the character of these structures as they evolve in both space and time. In some sense, each pixel of the high-speed camera can be thought of as a sensor capturing the intensity of the second derivative of the density gradient with respect to space as it varies with time. It is a straightforward matter to apply traditional signal processing and analysis techniques to these pixel time histories in order to generate insight into an otherwise extraordinarily complex dataset. The methods discussed in the following are typical applications of statistical and frequency domain analysis with some discrete-time filtering applied to large datasets of images. Traditionally, these methods provide insight into the character of some process measured by a single sensor. In the context of the forthcoming discussion, the reader should keep in mind that these are traditional and well-established signal processing and analysis techniques. Perhaps the only novelty in the following is that the number of sensors is large (pixel array of camera sensor) and the processes complex.

In addition to the dual shadowgraph data systems, the Ames UPWT possesses an advanced infrared flow visualization capability. Consisting of high sensitivity, megapixel mid-wave infrared cameras and unique contrast enhancement algorithms, this system is capable of providing real-time imaging of surface flow features. These flow features include boundary layer transition, shock impingement, flow separation, and buffet. Infrared imagery was captured during a subset of these wind tunnel tests corresponding with the unsteady pressure sensitive paint measurements. The primary goal of these measurements was to record the variation in temperature across the wind tunnel model, providing a dataset to temperature correct the unsteady pressure sensitive paint. Any flow features visualized using the infrared technique were secondary objectives, yet will be the subject of discussion in the following.

---

[*] Aerospace Engineer, Wind Tunnel Systems Branch, MS 227, Member AIAA
[†] Aerospace Engineer, Wind Tunnel Systems Branch, MS 227
[‡] Aerospace Engineer, Experimental Fluid Mechanics Branch, MS 260, Member AIAA

American Institute of Aeronautics and Astronautics

II. Experimental Setup

The following imagery and analysis were taken from two wind tunnel test entries spanning multiple model configurations and scales of the SLS at the NASA Ames UPWT. For simplicity we will examine only a few of these configurations and limit the results and discussion to data taken in the 11-by-11 foot test section. We will briefly discuss these data systems but more details can be found in Lee [2] and Garbeff et al. [3].

A. Facility and Test Articles

The following discussion will be limited to two model scales and will be generally referred to as SLS model configurations 1 and 2. In reality these two model configurations reflect two separate wind tunnel test entries. The test objectives of *configuration 1* was to characterize the performance of the SLS in crewed and payload configurations. The test objectives of *configuration 2* was to characterize the aeroacoustic environment of the SLS for several different geometries. Figures 1 and 2 detail these configurations installed in the 11-by-11 foot NASA Ames UPWT test section. The red circle approximates the location of the mirrors used to collimate the light for the shadowgraph measurement. The green rectangles represent the field-of-view of the camera with respect to the wind tunnel test section. The location of the test section window frame support structure and slotted wall baffles (horizontal and vertical lines) should be noted as they will likewise appear as dark bars in the image data. During a portion of testing for model *configuration 2* the test article was coated with fast-response pressure-sensitive paint. In an early effort to provide a measurement for temperature compensation, an IR camera was installed in the ceiling. These configurations were chosen for the following discussion as they represent two different scales of the SLS and therefore afford differing effective fields-of-view of the flow field.
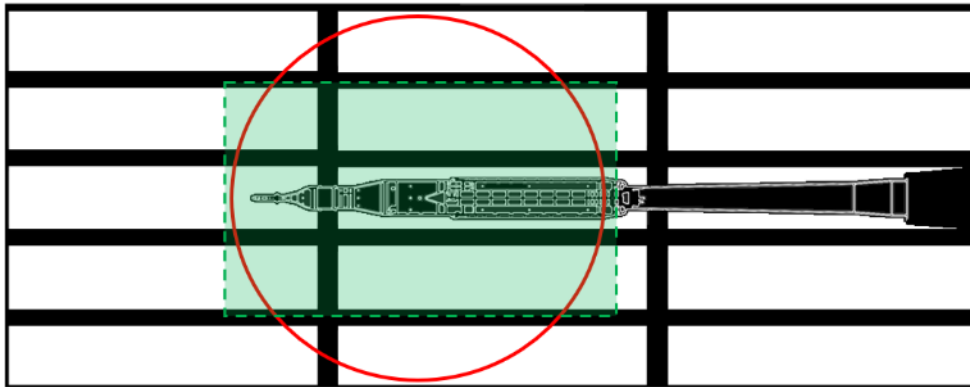

Figure 1: SLS model *configuration 1* in 11-by-11 foot UPWT test section
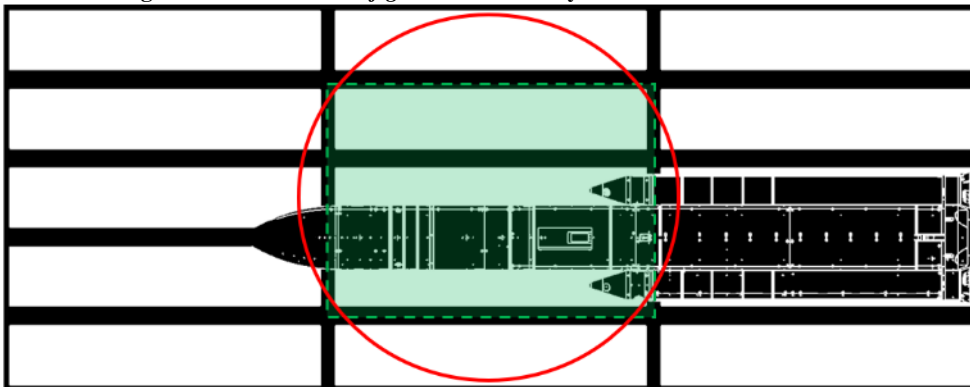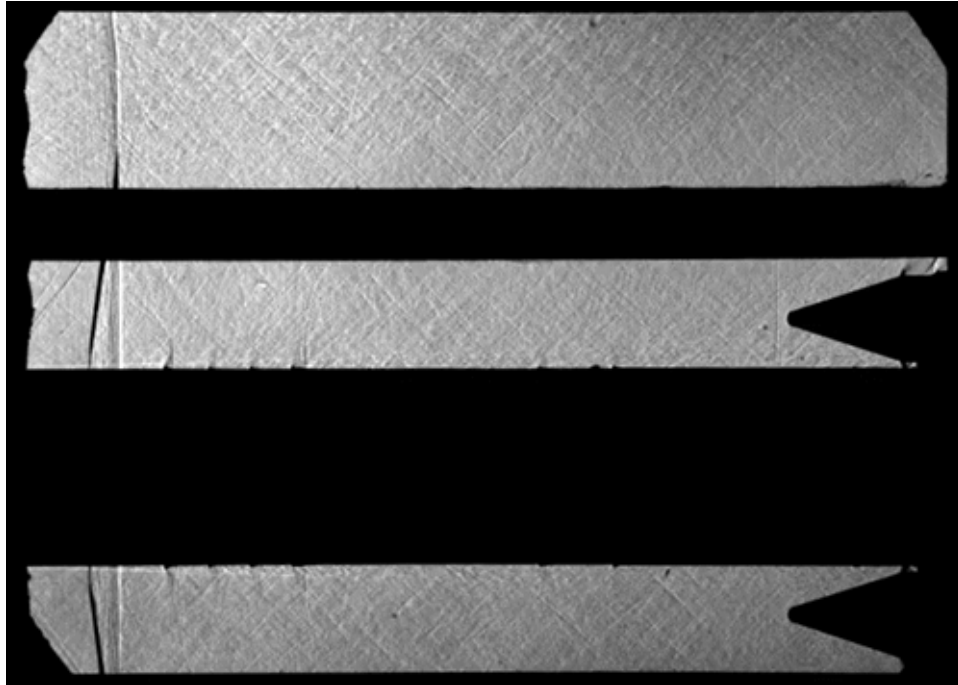

Figure 2: SLS model *configuration 2* in 11-by-11 foot UPWT test sections

B. Time Resolved Shadowgraph

The NASA Ames UPWT shadowgraph system is a classic Z-type setup consisting of a high-powered LED source, two light collimating four-foot diameter mirrors, optical quality test section glass, digital cameras with associated optics and data systems [3]. Shadowgraphy is performed for the majority of testing at the Ames UPWT, as it is more sensitive to the gradients produced by shock waves and fine scale turbulence [4]. The following discussion will be limited to the image data from the high-speed camera. This camera was a Phantom v2511 series high-speed camera with acquisition parameters on the order of 50,000 frames per second (FPS), and four microsecond exposure times. Shadowgraph Image data was captured over a Mach number range of $0.7 \leq M \leq 1.3$ at various angle-of-attack and roll configurations. Optical access at the 11-by-11 Ft test section is limited by the rectangular window frames and slotted wall baffles (see Figures 1 and 2). Figure 3 details a shadowgram of *configuration 2* of the SLS wind tunnel model at transonic conditions in the 11-by-11 foot test section. As the flow accelerates around the inter-stage adapter a lambda

2

American Institute of Aeronautics and Astronautics

shock forms (left portion of image). Flow disturbances due to the flanges on the center body disrupt the boundary layer and create regions of elevated fluctuations in the near-field. In addition to the flow features that are created by the presence of the model, there are phenomena visible in Figure 3 that are produced by the operation of a transonic wind tunnel. These features are produced by acoustic phenomena driven by the slotted test section walls (slot tones) and blade pass frequency of the three-stage compressor (drive tones). Taken together, these flow features occur at different scales in space and time creating an information rich dataset that can often be overwhelming to the observer.

Figure 3: Example Shadowgram of *Configuration 2* in the 11-by-11 foot test section

C. Infrared Imaging

A FLIR SC8200 series mid-wave (3-5 µm), research grade infrared (IR) camera was positioned to image *configuration 2* of the SLS model during the portion of testing dedicated to fast-response pressure-sensitive paint. The model SC8200 is a megapixel (1024x1024) mid-wave IR camera that is most commonly deployed at the Ames UPWT for infrared flow visualization purposes [5]. The exposure time of an IR camera is dependent upon the radiance expected within the image field. Given the range of total temperature (typically 50-90 ºF) of the 11-by-11 foot facility, exposure times for the SC8200 series camera are on the order of 6 milliseconds. The primary goal of this measurement was to provide a dataset to explore the temperature sensitivity of the fast-response pressure-sensitive paint. As an absolute measurement of temperature, the uncertainty of IR image data was high as the fast-response pressure-sensitive paint possesses a low-emissivity. A low-emissivity surface results in an image dominated by background reflections [6] making it difficult to remove the true temperature of the test article surface from the temperature of the surrounding test chamber. A series of flush mounted thermocouples were installed to provide a local measurement of temperature. The correction and analysis of the IR image data as a measurement of absolute temperature is beyond the scope of the current discussion. In the following, the IR image analysis discussion will be limited to relative temperature gradients with relevance to visualizing flow features.

III. Data Analysis and Processing Methods

As evidenced in Figure 3, the unprocessed results of shadowgraph imaging in a transonic wind tunnel are information rich and can be difficult to interpret. Therefore, the methods used to analyze and process these datasets should seeks to simplify the image data while extracting meaningful information. To that end we apply statistical and frequency domain data analysis techniques on a pixel-by-pixel basis across time. A useful result of the statistical image analysis is a data product based on the standard deviation of each pixel time history. This has the feature of both cleaning up non-stationary processes (transverse slot tone and drive tone waves) and detailing the character of stationary processes (boundary layer growth, flow separation, and shock wave geometry). In a similar fashion, frequency domain analysis can be applied to these datasets on a pixel-by-pixel basis. These results reveal the frequency content of various flow structures and compliment unsteady surface pressure measurements by providing context as to the fluid-structure interaction driving the surface measurements. The periodograms produced by this analysis have a quantitative aspect to them and help guide further processing techniques that reveal the physical character of flow features in the image data.

American Institute of Aeronautics and Astronautics

A. Statistical Images

A set of "statistical images" can be produced by computing the mean and standard deviation at each pixel location across time for each high-speed burst of images. For time-resolved shadowgraph this produces a data product that is both visually cleaner and able to reveal qualitative aspect of the flow field that would perhaps go unnoticed in the raw image data. Figure 4 details a set of statistical images computed from high-speed shadowgraph image bursts taken at subsonic (left) and supersonic (right) flow conditions. The top set of images in Figure 4 show a single instance in time (snapshot) taken from the high-speed image burst. At subsonic conditions (left) there are no obvious flow features, while the snapshot taken at supersonic conditions (right) details the shockwave geometry generated by the vehicle as well as the transverse waves (slot tones and drive tones) that are produced through the operation of the wind tunnel. The middle set of images depict the result of computing the mean of each pixel time history from the aforementioned datasets. Once again at subsonic conditions there are no obvious flow features. At supersonic conditions the effect of computing a mean image is that the non-stationary transverse waves have been averaged out. The result is a cleaner looking image highlighting the stationary processes (shock geometry). Finally, the bottom set of images detail the result of computing the standard deviation of each pixel time history of the original dataset. An intensity preserving color scheme [7] has been used to produce a pleasing image that conveys the complexity of the result. Now when examining the results computed from the subsonic dataset, we can clearly see brighter region corresponding to separated flow behind the nozzles of the launch abort tower. Additionally, growth of the boundary layer can be followed as bright regions along the outer-mold-line (OML) of the vehicle. Similarly, the results computed from the supersonic dataset identify strong and weak shocks as well as the boundary layer along the OML of the vehicle. These statistical images, and particularly the images of standard deviation, produce a concise result that qualitatively describes the extent and behavior of many of the flow features generated by the vehicle.
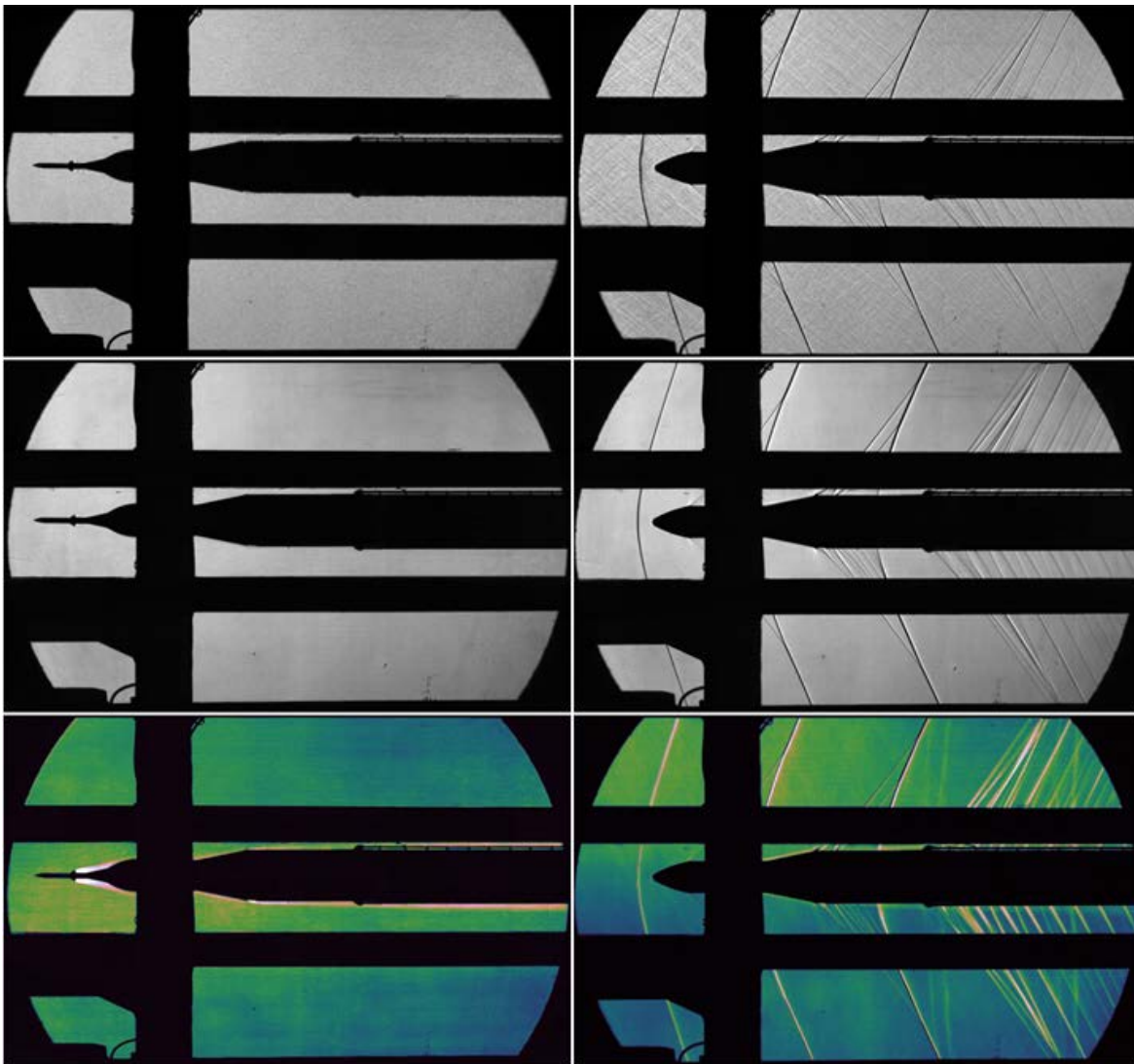

Figure 4: *Configuration 1* **subsonic (left) and supersonic (right) high-speed shadowgraph statistical image analysis: single snapshot in time (top), mean (middle), standard deviation (bottom)**

American Institute of Aeronautics and Astronautics

B. Frequency Domain Analysis and Discrete-Time Filtering

In a similar fashion to the statistical analysis of section A, frequency domain analysis can be applied to the image time histories on a pixel-by-pixel basis. These results reveal the frequency content of various flow structures and compliment unsteady surface pressure measurements by providing context as to the fluid-structure interaction driving the surface measurements. For a given dataset a periodogram is produced by implementing Welch's method [8] on a pixel-by-pixel basis. The energy at each pixel location for a fixed frequency is summed across all pixels in the image resulting in a periodogram of total image energy versus frequency (Figure 5). These periodograms give insight into the time scales that dominate the flow field. A powerful aspect of this technique is that for each frequency of the periodogram, an image of the energy distribution at that specific frequency can be computed. Each instance of the frequency map relates flow features in the dataset corresponding to that frequency. This is demonstrated in Figure 6 where two separate instances of the frequency map are taken from a given periodogram. The vertical line on each periodogram on the lower portion of each image indicates what frequency the image represents. It can then be inferred that the structures present in the image contain the energy at that frequency. For example, Figure 6 details the frequency map images related to two peaks in the periodogram of Figure 5. The left-hand image corresponds to a sharp peak in the periodogram and appears to be associated with downstream shock structures. The right-hand image corresponds to the broader, higher frequency peak and is associated with the slot tones produced by the tunnel. A useful representation of the full frequency map is to compile each frequency map image into a movie, where each frame of the movie represents a fixed frequency. These frequency maps have a quantitative aspect to them and help guide further processing technique that reveal the physical character of flow features in the image data. For instance, upon identifying a frequency band of interest a discrete-time filter can be designed and applied to the original dataset. This provides insight into the physical processes that contribute to a given frequency (or frequency band).
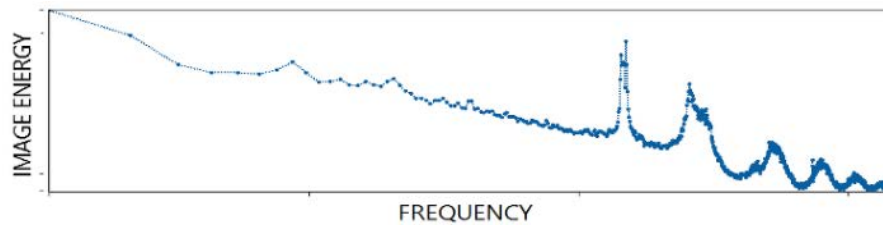

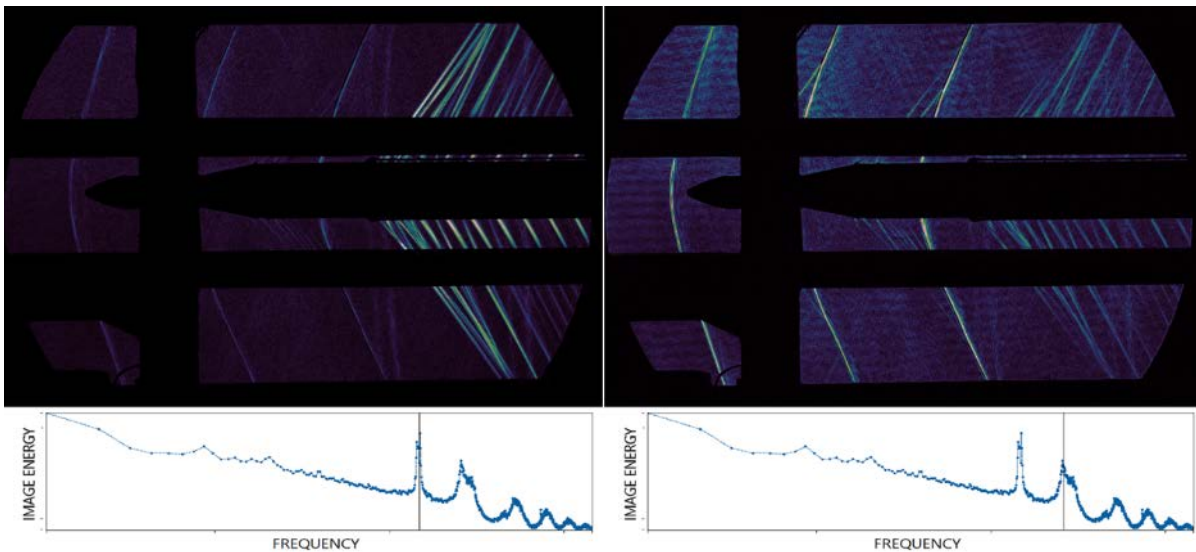**Figure 5: Periodogram of high-speed shadowgraph image burst**

Figure 6: Two frequency map images of a computed periodogram

5

IV. Results and Discussion

In the following section we will apply the aforementioned analysis and processing methods to the high-speed shadowgraph and IR image data. The bulk of the discussion will address the high-speed shadowgraph results as the primary goal of this measurement (and the emphasis of this paper) was to visualize the flow field of the SLS throughout a range of Mach numbers. To that end, the statistical image analysis, and the images of standard deviation in particular, provide a concise method of visualizing a wide variety of flow phenomena. Some of the phenomena to be discussed will range from separated flows, to large complex shockwave geometries, to shock-induced separation events. Selected frequency domain analysis results with respect to the high-speed shadowgraph will then be discussed and a few applications of discrete-time filtering demonstrated. This method of discrete-time filtering guided by frequency domain analysis will then be applied to an IR image dataset, revealing hidden flow features in an otherwise uninteresting (from a flow visualization perspective) dataset.

A. High-Speed Shadowgraph Statistical Image Analysis

We will begin by examining the high-speed shadowgraph statistical image analysis data products. For brevity, the discussion will be limited to images of pixel time history standard deviation. As demonstrated in section 3a, this data product is an effective means of visualizing the qualitative character of the flow field generated by the launch vehicle. When taken together, Figures 7, 8, and 9, depict *configuration 2* in increasing Mach numbers from subsonic to supersonic (flow is left-to-right). Each image itself has been computed from a high-speed burst taken at a fixed Mach number. In the first few images of Figure 7, the effect of the flanges on the flow field around the vehicle center core appears as bright regions of separated flow in that area. As the Mach number increases a small lambda shock forms at the most upstream flange followed by a larger lambda shock occurring at the junction between the nose cone and center core. Figure 8 details the transition from transonic flow to supersonic flow for *configuration 2*. Each flange of the center core generates a shock structure that varies to some degree from its neighbor. This is likely due to the variation of the state of the boundary layer creating a unique shock-boundary layer interaction at each streamwise location. In the second, third, and fourth frames of Figure 8 a large vertical feature appears, defining the strong normal shock structure as the vehicle passes through the transonic regime. In the final two frames of Figure 8 the flow field is supersonic and is characterized by a complex geometry of shockwave features now including the bow shocks of the solid rocket boosters (SRBs). In the final frame of Figure 8 two shocks can be seen emanating from outside the field of view. The sources of these shocks are likely the edges of window frames in the floor and ceiling of the test section. Figure 9 shows a progression of images as the Mach number increases in the supersonic flow regime. A curving vertical shock has appeared and moves downstream with Mach number. This feature is not local to the vehicle but rather the bow shock of the most upstream portion of the vehicle intersecting the test section of the windows, a consequence of the fact that this technique integrates across the entire light path. As expected, with increasing Mach number the shock wave angle decreases accordingly.

Figure 10 depicts a coarser Mach sweep of *configuration 1*. Since *configuration 1* is a smaller scale than *configuration 2* (see Figures 1 and 2) these views afford a wider effective field-of-view. The first three frames of Figure 10 detail the progression through the transonic regime. Small shocks form at OML changes between the center core and SRB nose cones, and inter-stage adapter. These regions correspond to favorable pressure gradients where the flow accelerates forming a local shock. A shock induced separation event can be seen downstream of the small shock forming at the inter-stage adapter. In the final three frames the character and development of the bow shock of the entire vehicle can be observed, as well as the many small shocks emanating from features attributed to the OML of the center core and SRBs. In a similar fashion to Figure 9, bow shocks intersecting the test section windows appear as faint vertical lines in the fourth image of Figure 10. In the final image, diagonal shocks emanating from outside the field of view can be seen intersecting just above the centerline of the test section. The location and geometry of these shocks are nearly identical to the final image of Figure 8 providing confirmation that these features are likely unique to the test section floor and ceiling window configurations rather than local to the wind tunnel model.
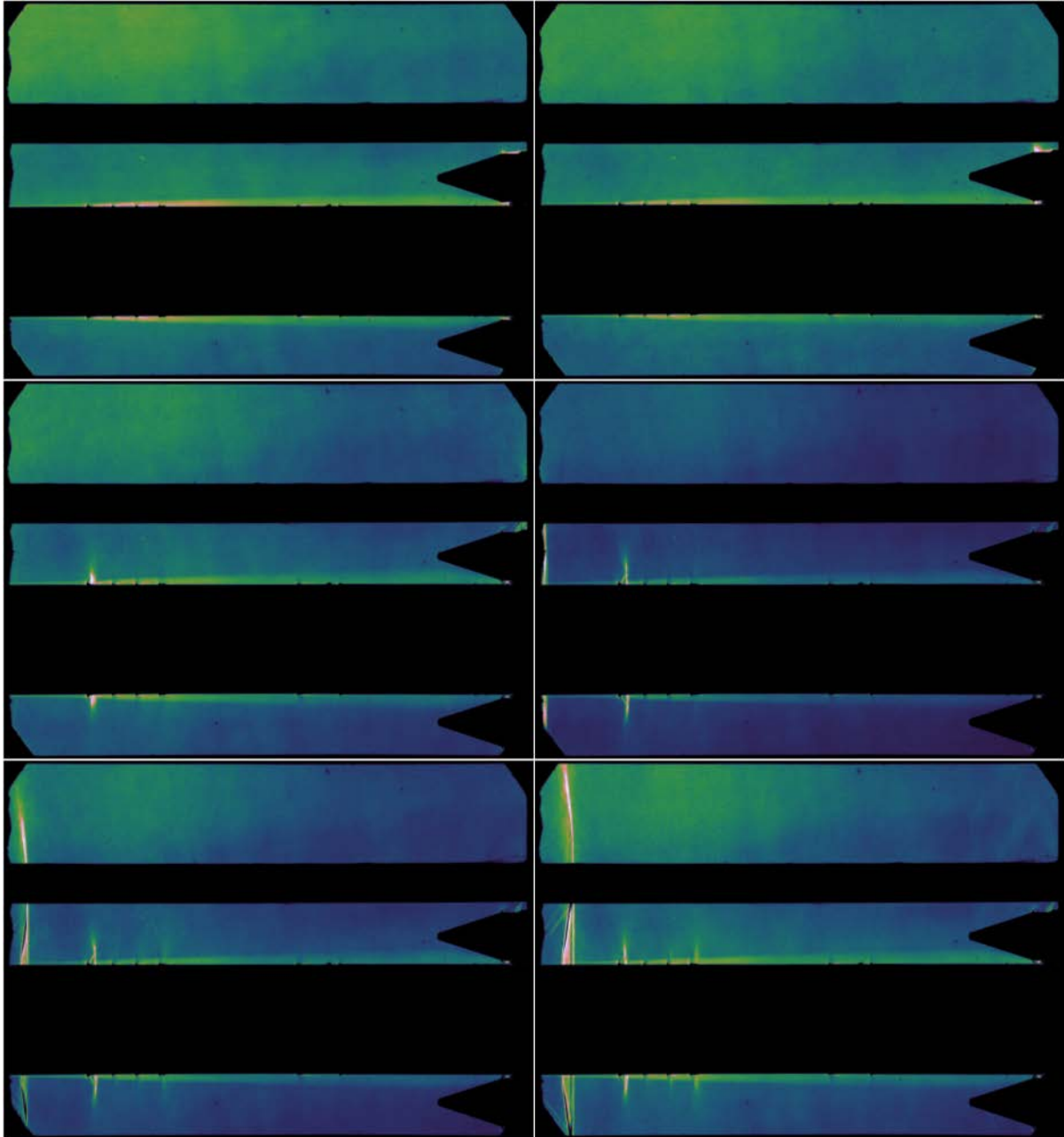
Figure 7: High-speed shadowgraph standard deviation images, *configuration 2***, subsonic to transonic Mach number sweep (left to right, top to bottom)**

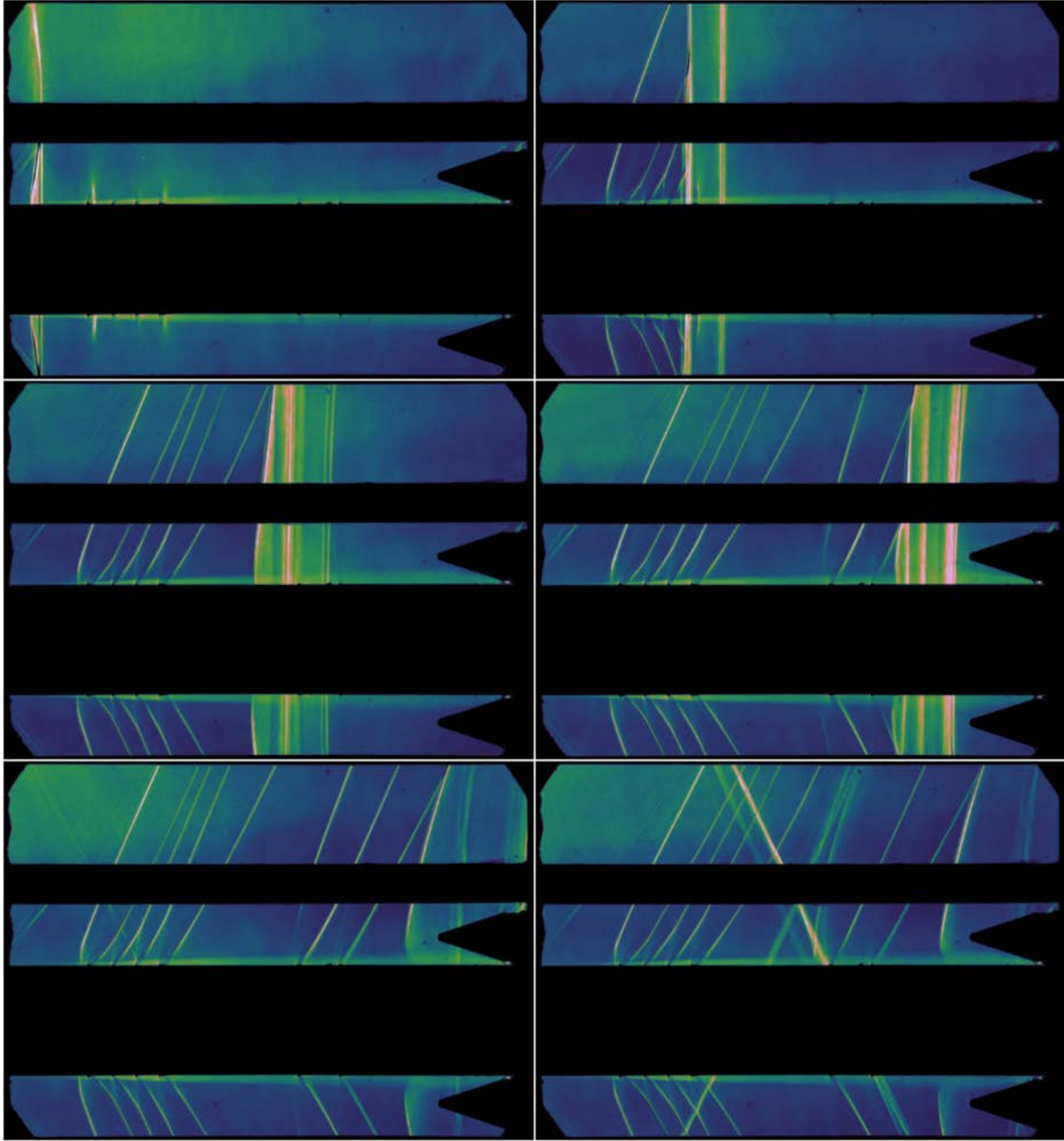American Institute of Aeronautics and Astronautics

Figure 8: High-speed shadowgraph standard deviation images, *configuration 2*, transonic to supersonic Mach number sweep (left to right, top to bottom)
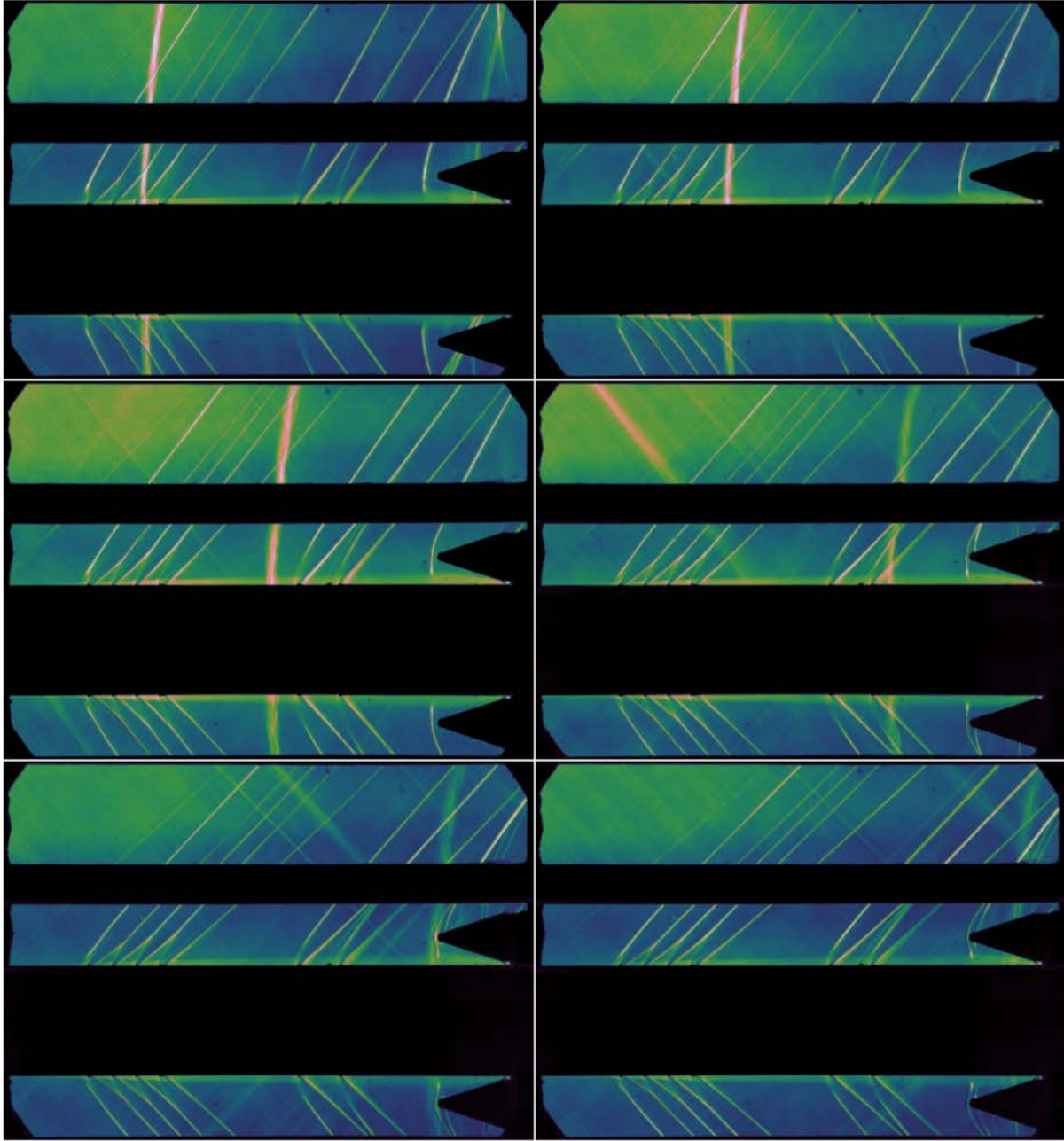
American Institute of Aeronautics and Astronautics

Figure 9: High-speed shadowgraph standard deviation images, *configuration 2***, supersonic Mach sweep (left to right, top to bottom)**

American Institute of Aeronautics and Astronautics
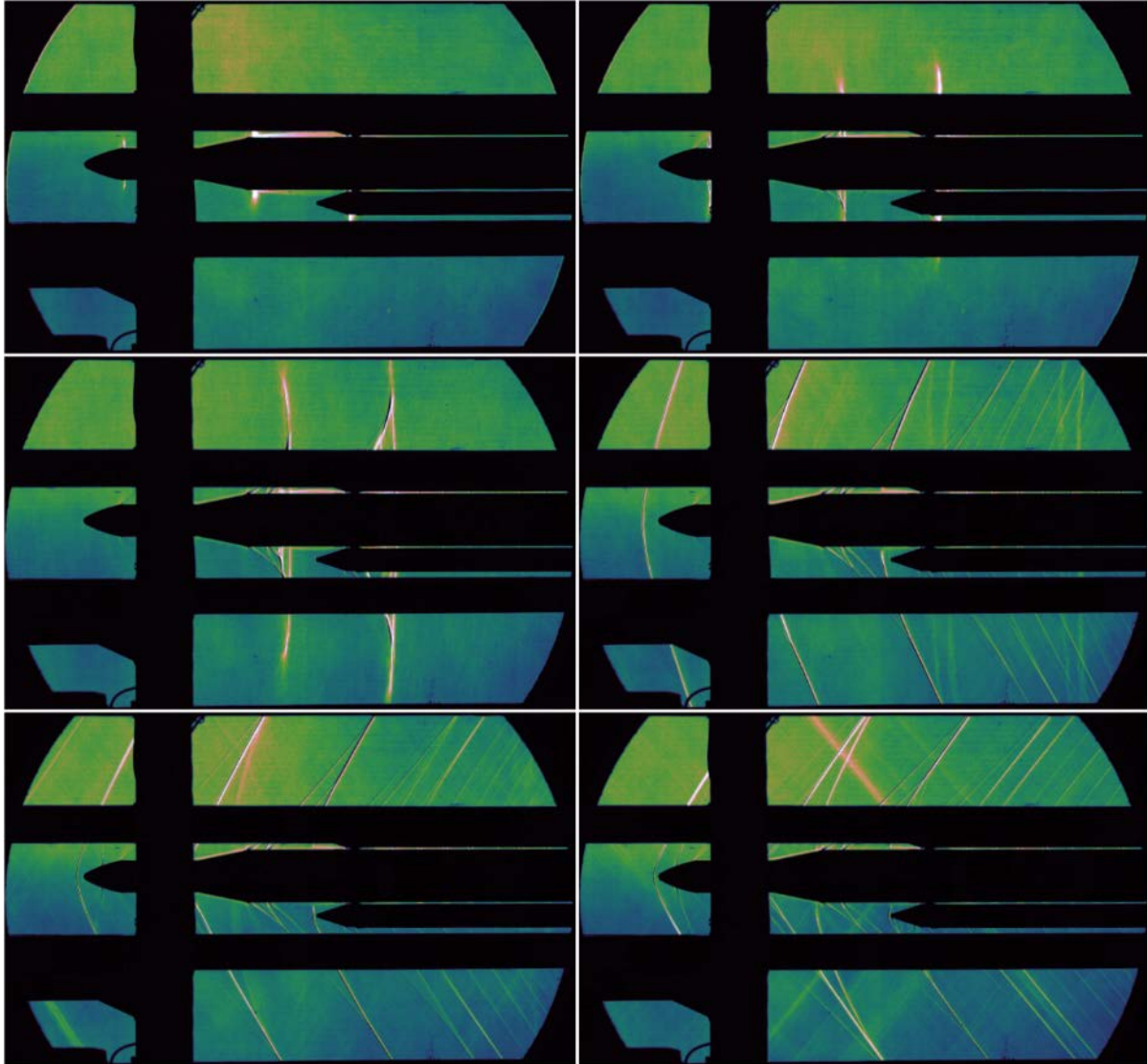
Figure 10: High-speed shadowgraph standard deviation images, *configuration 1* **Mach sweep (left to right, top to bottom)**

B. High-Speed Shadowgraph Frequency Domain Analysis and Discrete-Time Filtering

In this section we will examine the results of performing frequency domain analysis on a subset of SLS high-speed shadowgraph data. The periodograms and frequency maps produced by this analysis reveal the frequency content that makes up each burst of images. Figure 11 shows a series of periodograms of SLS *configuration 1* computed from high-speed image bursts taken at a fixed angle-of-attack with varying Mach number that increases from top (lowest Mach) to bottom (highest Mach). The first three periodograms are largely subsonic and transonic while the last three are taken from supersonic data. The supersonic periodograms contain an order of magnitude more energy at the lower frequencies than the subsonic ones. The wind tunnel model and imaging systems are subject to higher levels of vibration throughout this frequency range due to the operation of the wind tunnel. The supersonic periodograms are also defined by several sharp peaks in the high-frequency band. The first and sharpest of these peaks looks to be frequency content inherent in the downstream shock structure and will be examined in detail in the upcoming discussion. The subsequent broader peaks occurring at higher frequencies are related to the primary and harmonic frequencies of the slot tones of the wind tunnel test section (see right-hand image of Figure 6). The final (most bottom) periodogram of Figure 11 depicts the highest Mach number achieved for this test series. Its periodogram frequency content follows a pattern similar to the other supersonic periodograms but differs in that a broad, low-frequency bump is now apparent. This feature will be examined in the upcoming discussion.

10
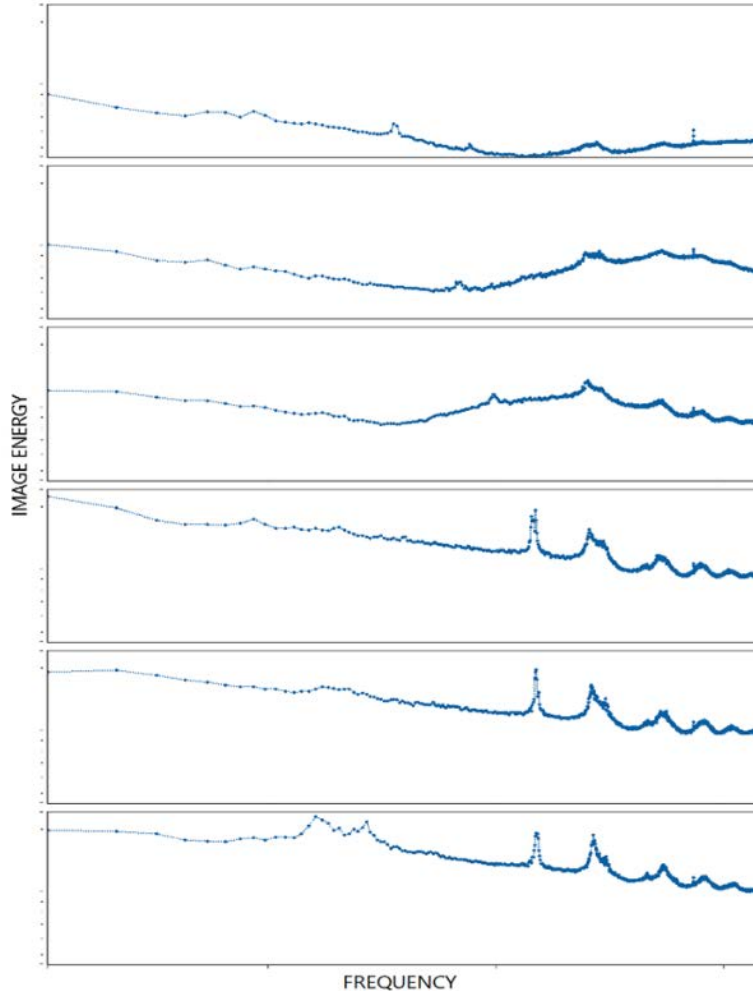
Figure 11: Mach number sweep periodograms (Mach number increases from top to bottom)

Next we will examine the nature of the sharp peak that appears in the supersonic periodograms of Figure 11. When comparing periodograms computed at two different Mach numbers across two model roll orientations, it is apparent that this feature is dependent on the orientation of the model with respect to the shadowgraph integration path. The two different model roll orientations are shown in Figure 12 for reference. The periodograms *a* and *c* of Figure 12 correspond to two Mach numbers with the model rolled so that the solid rocket boosters SRBs are shadowed by the center core of the vehicle. Conversely the periodograms *b* and *d* of the same figure correspond to a roll angle such that the SRBs are in view. When comparing the periodograms at a fixed Mach number with differing roll configurations the results look similar except for the sharp peak in question. Therefore it can be deduced that the frequency content of this flow feature is not symmetric and potentially associated with the liquid oxygen supply line running along the main core of the vehicle. Figure 13 depicts the four periodograms at a fixed Mach number with varying angle of attack. Periodograms *a* and *d* of Figure 13 were computed from data taken at angles-of-attack greater than 5 degrees whereas periodograms *b* and *c* were taken from data at 3 degrees and 0 degrees angle-of-attack respectively. The peak in question has begun to form by periodogram *b* and is well defined at periodogram *c* but is non-existent in periodograms *a* and *d*. Therefore, it can be implied that the feature is dependent upon angle-of-attack. Finally we examine the frequency map images (Figure 14) to locate the structures in the image data that are contributing to this peak in the periodogram. Figure 14 clearly shows high amounts of energy concentrated in the downstream shock structures. With these results in mind we can then conclude that there is a fluid-structure interaction driving a periodicity in the shock structures produced at an OML feature on the main core of the vehicle and that the magnitude and frequency of this phenomenon is dependent on Mach number and angle-of-attack.
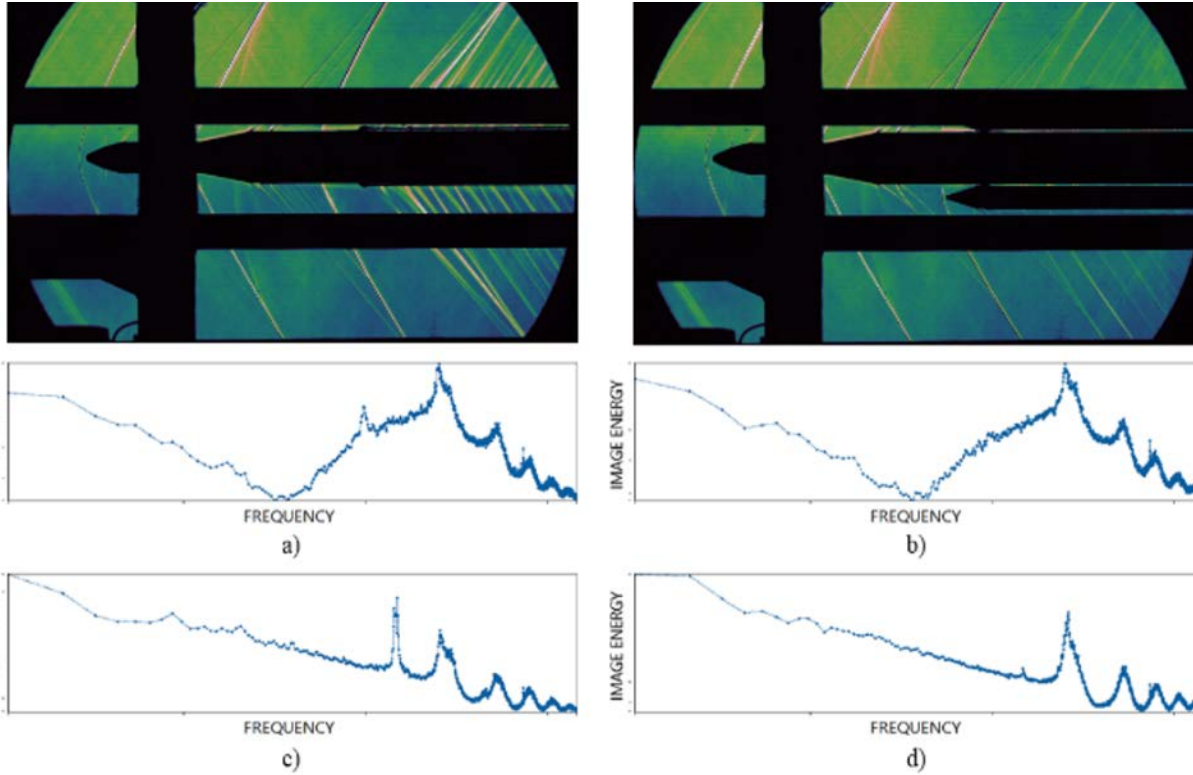
Figure 12: Periodograms at two Mach numbers (Mach number case one (a, b) and two (c, d), SLS rolled with SRBs shadowed by main core (a, c), and in view (b, d)
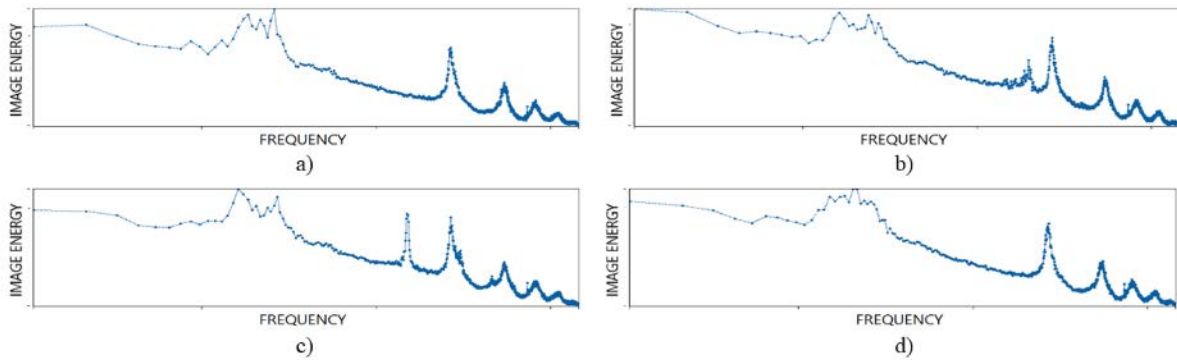

Figure 13: Periodograms at fixed Mach number with varying angle-of-attack

American Institute of Aeronautics and Astronautics
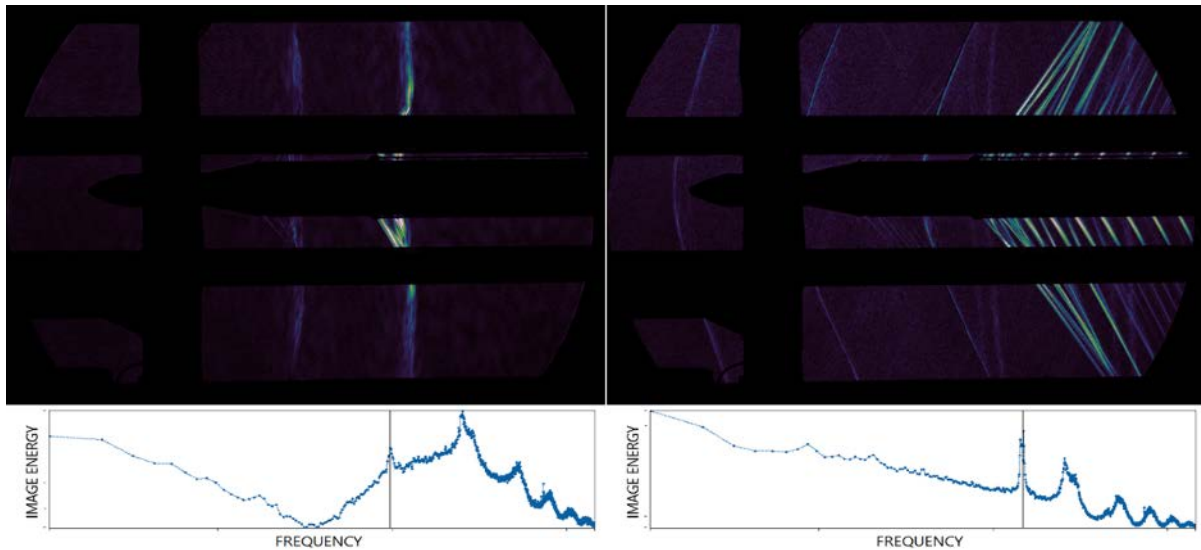
Figure 14: Frequency map images of sharp peak, two Mach numbers (transonic and supersonic)

As discussed previously, there exists a broad hump of low frequency energy present in the high Mach number (most bottom) periodogram of Figure 11. In order to gain some insight into the mechanism causing this feature we examine a frequency map image (Figure 15) taken at a frequency where the phenomenon is occurring. Figure 15 shows that much of the energy at this frequency is concentrated in the strong shock features associated with the nose and major OML changes of the vehicle. This feature is also present in the periodograms of Figure 13 and looks to be largely independent of angle-of-attack. The authors are unsure of a flow mechanism that would produce a broad periodicity in this frequency range for these shock structures. However, based on the previous analysis we can conclude that this feature is highly Mach number dependent (only occurring at the highest Mach conditions), not dependent upon angle-of-attack, and is most concentrated in the strong shock features (not as present in the weaker downstream shocks). When closely examining Figure 15 it may be concluded that the energy in strong shock features decreases as it nears the vehicle. This implies that phenomenon may not be driven by the fluid-structure interaction at vehicle surface but rather by some mechanism away from the vehicle.
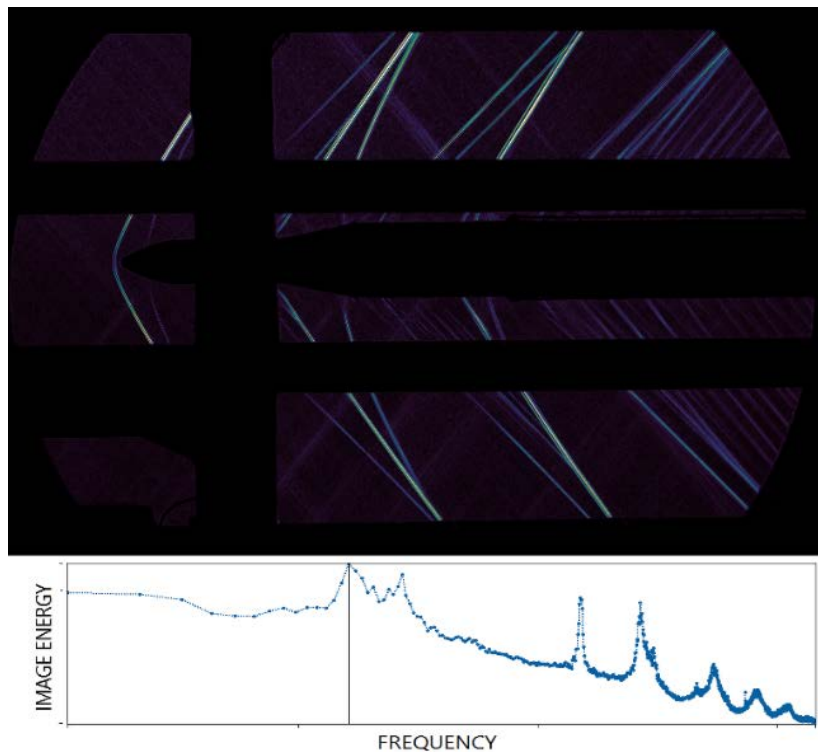

Figure 15: Frequency map image of broad, low-frequency hump

13

With the ability to analyze the frequency content of these complex flow fields a processing method based on discrete-time filtering can be applied to the raw data. The result is a new time series that emphasizes a particular frequency (or frequency band). This helps simplify the image data but can also reveal hidden features in the flow. Figure 16 demonstrates a comparison between unfiltered and filtered image data for the low frequency band. Here it is clear that the strong shock features are major contributors to the energy occurring in this frequency band. Conversely, the high-frequency filtered data identifies the features in the flow field contributing to that band. This can be seen in Figure 17, where the filtered image is now dominated by the many transverse waves associated with the slot tones of the test section wall. To reiterate, each of these filtered images are derived from the same original dataset, this process has only separated what flow features are happening at different frequencies.
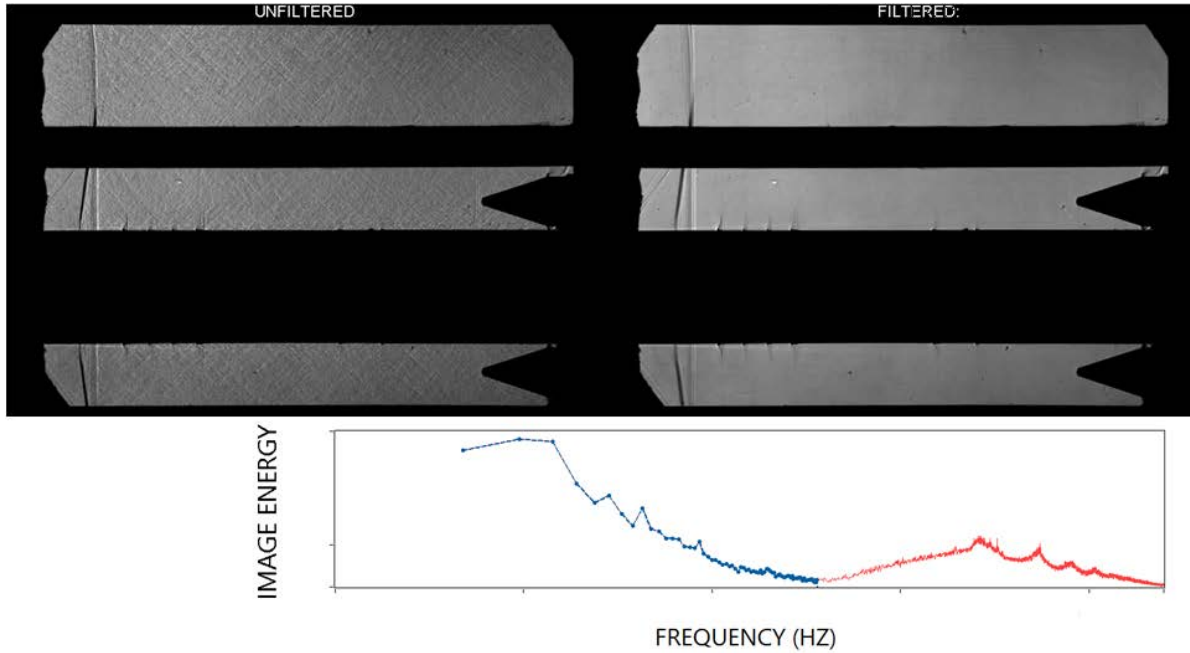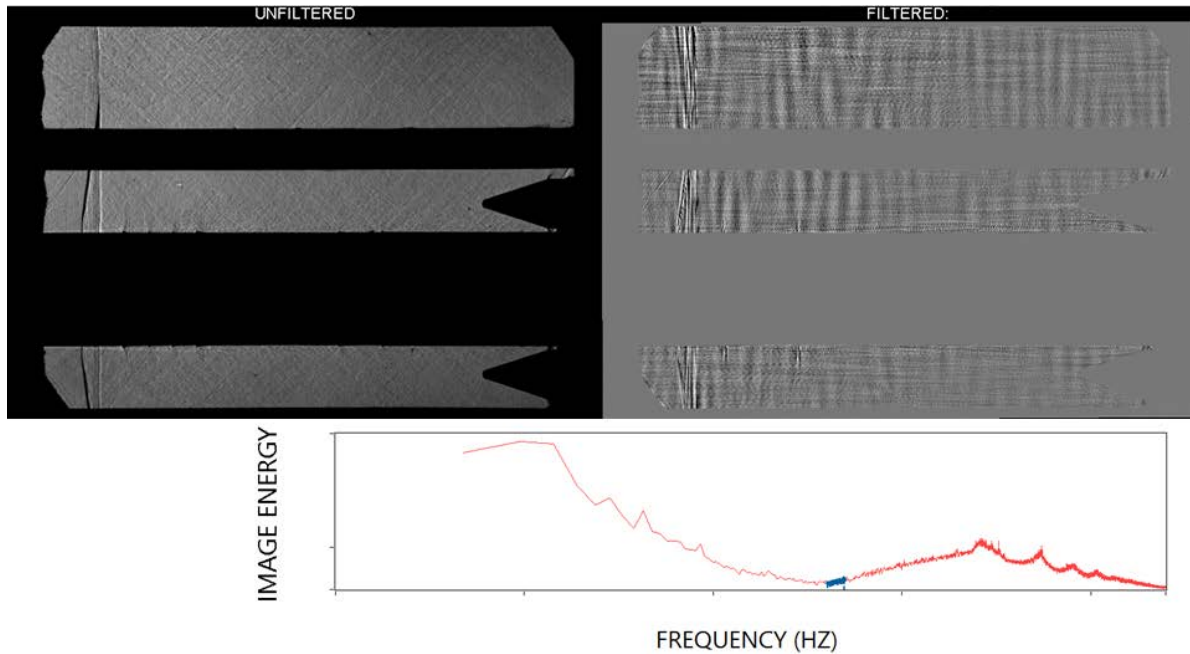

Figure 16: Discrete-time filter image comparison: low-pass (blue portion of periodogram, right-hand image)
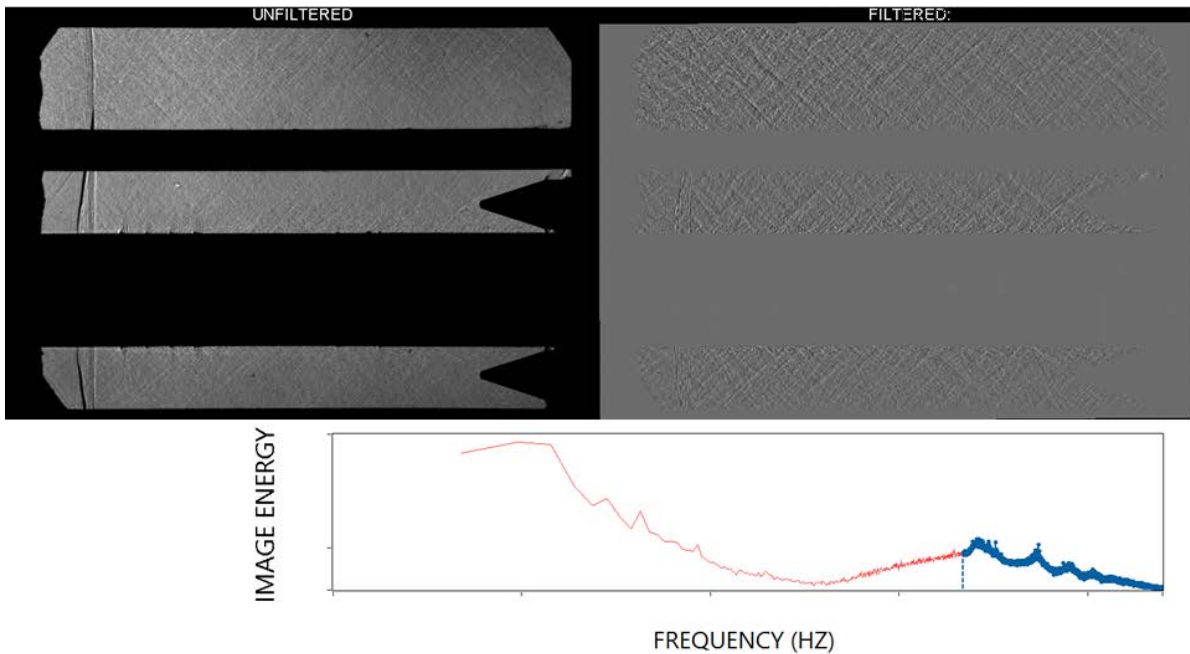
Figure 17: Discrete-time filter: high-pass (blue portion of periodogram, right-hand image)

American Institute of Aeronautics and Astronautics

Filtering the high-speed shadowgraph data also creates the ability to reveal features in the flow field that may otherwise be hidden. For example, given a drive speed, the blade pass frequency of the 11-by-11 foot three stage compressor can be estimated. This blade pass frequency produces a measureable effect on the flow field. These drive tones have been well documented in both test sections using hot-wire anemometry and unsteady pressure transducers. In an attempt to visualize this drive tone frequency, a band-pass filter is applied to the image data in the same fashion as previously discussed. Figure 18 details the results of filtering the image data in this frequency range. In this filtered image the drive tones are manifested as vertical waves that propagate upstream. This demonstrates the power of this technique to reveal structure within the flow that would otherwise be hidden.


Figure 18: Discrete-time filter: band-pass (blue portion of periodogram, right-hand image)

C. Infrared Imaging Frequency Domain Analysis and Discrete-Time Filtering

Infrared flow visualization relies on resolving small temperature gradients on the surface of wind tunnels models that are imparted by some aerodynamic phenomenon. The ability to image these small temperature gradients is highly dependent on the heat transfer conditions between the free stream and test article as well as the emissivity of the wind tunnel model. For a wind tunnel model with poor emissivity or non-ideal heat transfer conditions, this leads to the signal of interest being hidden within a larger background signal. This makes infrared flow visualization an excellent candidate for the preceding frequency domain analysis. Therefore the frequency domain analysis and filtering tool was adapted to process high-bit depth infrared images, resulting in some unexpected results. Figure 19 details two images taken from a frequency map computed from a supersonic infrared time-series. The content in each image is separated by only a few hertz however the image on the left shows a shock structure around the vehicle while the image on the right does not. Applying a band pass filter to the original time series to select only the frequency content containing the shock features results in Figure 20. In this image the shock structure surrounding the vehicle is clearly evident yet is not visible in the original infrared image data.

15

American Institute of Aeronautics and Astronautics
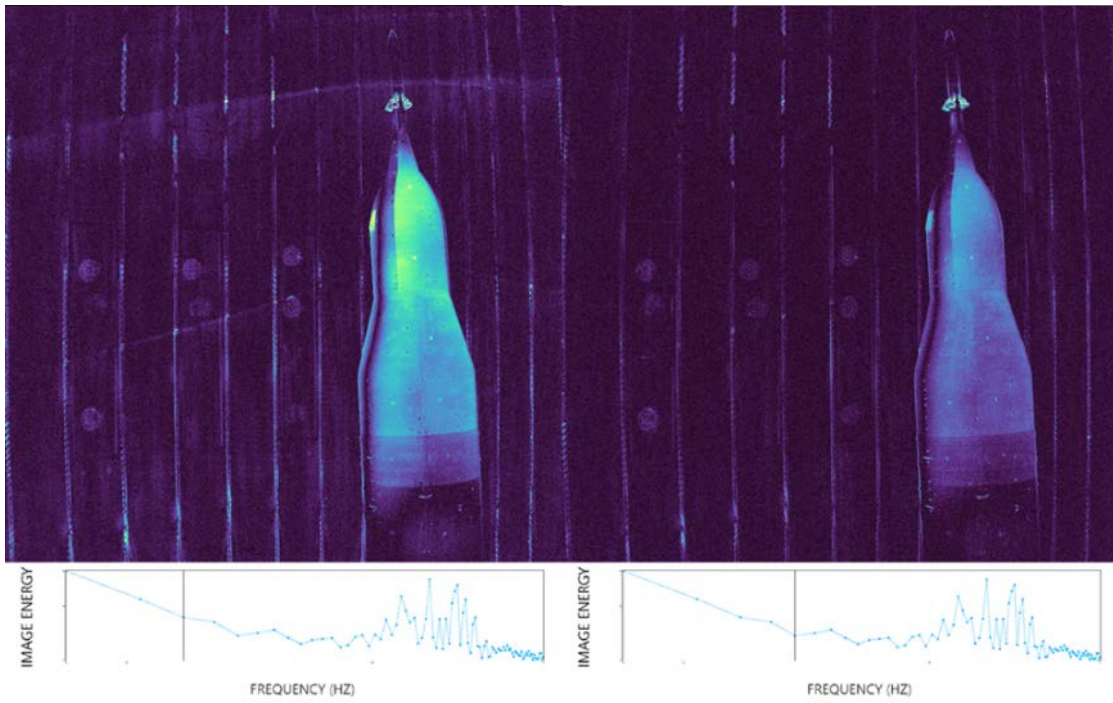
Figure 19: Two IR frequency map images
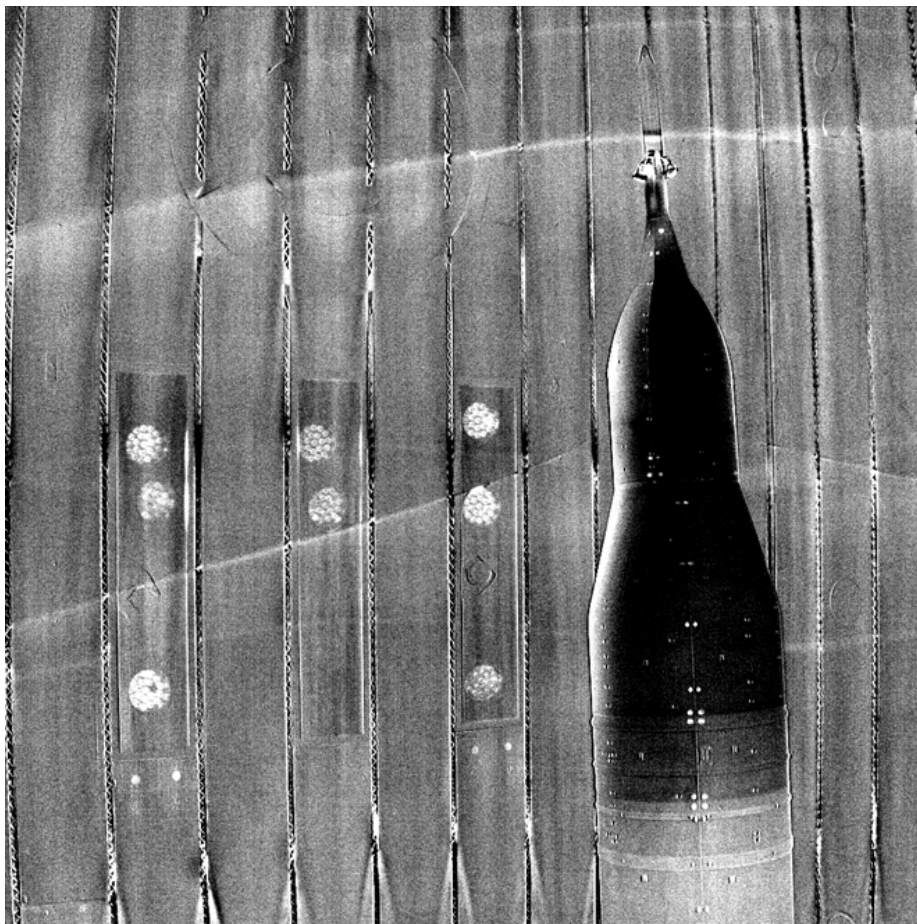
Figure 20: Band-pass filtered IR image revealing hidden shock structure

16

V. Conclusions

In the preceding discussion we have examined selected flow visualization results from two separate entries and model configurations of the SLS in the NASA Ames UPWT 11-by-11 foot wind tunnel. Much of this discussion focused on the high-speed shadowgraph data and the results produced by statistical and frequency domain analysis. The statistical image analysis, and the images of standard deviation in particular, provided a concise method of visualizing a wide variety of flow phenomena. Some of the phenomena identified were separated flows caused by the flanges of the center core, large shock structures that developed and varied with Mach number, a shock induced separation event at the inter-stage adapter, and stray shocks emanating from the test section floor and ceiling windows. The frequency domain analysis produced periodograms and frequency maps that had a quantitative aspect to them. With these results we were able to discuss some general trends regarding the distribution of the image energy in the frequency domain. We then explored a few specific features identified in the periodograms. In particular, a strong spike in energy at a relatively high frequency was determined to be related to a flow driven periodicity near a downstream OML feature of the center core of the vehicle. Guided by this frequency domain analysis, we then demonstrated how discrete-time filtering can help simplify an otherwise complex flow field and even reveal hidden features in the original data. This concept of revealing hidden flow features in information rich datasets was applied to IR image data recorded during a portion of supersonic testing concurrent with fast-response pressure-sensitive paint. On this dataset frequency domain analysis revealed a mode depicting shockwaves reminiscent of a shadowgraph image. A band-pass filter was applied to the original time-series to emphasize this mode and the resulting images provide a unique view of the flow structures surrounding the vehicle. In summary, it is hoped that these methods and results will provide context and help validate the tools and processes used to design the next generation of launch vehicles.

Acknowledgements

References

[1] Garbeff, T.J., et al, *"Experimental Visualizations of a Generic Launch Vehicle Flow Field: Time-Resolved Shadowgraph and Infrared Imaging"* 55th AIAA Aerospace Sciences Meeting, (AIAA 2017-1403)

[2] Lee, G., *"Study of Optical Techniques for the Ames Unitary Plan Wind Tunnels Part 1: schlieren."* NASA-CR-189951, 1992

[3] Garbeff, T.J, Heineck, J.T., et al, *"Institutional Schlieren: A Production-Level Wind Tunnel Test Measurement"* 53rd AIAA Aerospace Sciences Meeting, (AIAA 2017-1403)

[4] Settles, G.S., *Schlieren and Shadowgraph Techniques.* Springer-Verlag, New York, 2001

[5] Garbeff, T.J., Baerny, J.K., *"Recent Advancements in the Infrared Flow Visualization System for the NASA Ames Unitary Plan Wind Tunnels"*, 55th AIAA Aerospace Sciences Meeting, (AIAA 2017-1051)

[6] Vollmer, M., Möllmann, K.-P., *"Infrared Thermal Imaging: Fundamentals, Research and Applications"*, Wiley-VCH, Germany, 2010

[7] Green, D. A, *"A colour scheme for the display of astronomical intensity images"*, Bulletin of the Astronomical Society of Inia, 39, 289, 2010, (2011BASI...39..289G at ADS.)

[8] Welch, P. D., *"The use of Fast Fourier Transform for the estimation of power spectra: A method based on time averaging over short, modified periodograms",* IEEE Transactions on Audio and Electroacoustics, AU-15 (2): 70–73, doi:10.1109/TAU.1967.1161901

American Institute of Aeronautics and Astronautics